

SafeguardGS: 3D Gaussian Primitive Pruning While Avoiding Catastrophic Scene Destruction

Yongjae Lee
Arizona State University
Tempe, AZ 85281
ylee298@asu.edu

Zhaoliang Zhang
Johns Hopkins University
Baltimore, MD 21218
zzhan288@jh.edu

Deliang Fan
Arizona State University
Tempe, AZ 85281
dfan@asu.edu

Abstract

*3D Gaussian Splatting (3DGS) has made significant strides in novel view synthesis. However, its suboptimal densification process results in the excessively large number of Gaussian primitives, which impacts frame-per-second and increases memory usage, making it unsuitable for low-end devices. To address this issue, many follow-up studies have proposed various pruning techniques with score functions designed to identify and remove less important primitives. Nonetheless, a comprehensive discussion of their effectiveness and implications across all techniques is missing. In this paper, we are the first to categorize 3DGS pruning techniques into two types: **Scene-level pruning** and **Pixel-level pruning**, distinguished by their scope for ranking primitives. Our subsequent experiments reveal that, while scene-level pruning leads to disastrous quality drops under extreme decimation of Gaussian primitives, pixel-level pruning not only sustains relatively high rendering quality with minuscule performance degradation but also provides an inherent boundary of pruning, i.e., **a safeguard of Gaussian pruning**. Building on this observation, we further propose multiple variations of score functions based on the factors of rendering equations and discover that assessing based on **color similarity with blending weight** is the most effective method for discriminating insignificant primitives. In our experiments, our SafeguardGS with the optimal score function shows the highest PSNR-per-primitive performance under an extreme pruning setting, retaining only about 10% of the primitives from the original 3DGS scene (i.e., 10× compression ratio). We believe our research provides valuable insights for optimizing 3DGS for future works.*

1. Introduction

The emergence of Neural Radiance Fields (NeRFs) [1, 2, 27] has advanced photorealistic 3D reconstruction quality and opened new opportunity for quality enhancement

in various fields, such as computer vision [23, 41, 42], robotics [32, 43, 48], and extended reality [7, 36]. The key concept that enables NeRF to achieve photorealistic rendering is encoding 3D scenes with their view-dependent effects into a series of multi-layer perceptrons (MLPs) and synthesizing novel views using alpha-compositing with an appropriate volume sampling strategy (a.k.a. volumetric rendering). However, the deep MLP structure and the high-cost volumetric rendering technique result in substantial computational overhead, hindering prevalent adoption in real-time applications. This has prompted subsequent research to focus on developing specialized data structures [3, 10, 28, 44], sophisticated sampling strategies [19, 21, 29], and incorporating deferred rendering techniques [5, 16] in an effort to improve rendering efficiency.

The recent approach of 3D Gaussian Splatting (3DGS) [17] has demonstrated remarkable success in high-quality 3D scene reconstruction, achieving real-time, high-fidelity scene rendering. Unlike previous NeRF methods [27, 28, 44], which implicitly represent 3D scenes using MLPs with dedicated data structures, 3DGS explicitly models scenes with parameterized 3D Gaussian primitives. During rendering, these primitives are efficiently projected and rasterized onto the image plane, a process called Splatting [49, 50]. Their tile-based, differentiable renderer, using an alpha-blending technique, enables both photorealistic rendering and efficient primitive optimization.

Despite the diligent efforts of 3DGS to maximize rendering efficiency, it still falls short due to the challenge of primitive booming. During the densification stage, where primitives are cloned and split to rectify erroneously reconstructed regions, the primitives often proliferate excessively, resulting in an overwhelming increase in their number. This explosive growth places heavy demands on computer memory, causing longer rendering latency especially on low-end devices. As noted by Fan et al. [8], most of these primitives contribute little to the rendered output and can be removed without impacting quality. Recognizing this, several recent studies [8, 9, 20, 24, 31] have proposed various Gaus-

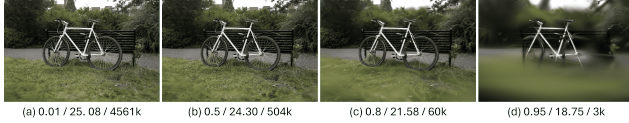


Figure 1. An incautious selection of pruning settings can lead to unexpected scene degradation. We reproduce (a)-(d) using the pruning technique from RadSplat [31], applied at 20k out of 30k iterations during primitive optimization. The caption of each image indicates importance score threshold (primitives below this are pruned), PSNR, and the number of primitives (Best viewed in zoom).

sian primitive pruning techniques that assess the importance of each primitive and eliminate those that are insignificant. However, these techniques have not been thoroughly investigated, leaving the risk of substantial quality degradation when pruning settings are not carefully selected, as illustrated in Fig. 1.

In this paper, we propose SafeguardGS, which inherently imposes a natural limit on the pruning settings, which prevents catastrophic scene destruction, and demonstrates superior performance under extreme pruning conditions compared to existing techniques. Initially, through a thorough examination of existing Gaussian primitive pruning techniques, we identify two major pruning categories: *Scene-level pruning*, which ranks primitives in a global context, and *Pixel-level pruning*, which ranks primitives in an individual ray context. Interestingly, our preliminary experiment reveals that pixel-level pruning outperforms scene-level pruning in general. Additionally, it suggests that pixel-level pruning inherently indicates a minimum boundary for the number of primitives; surpassing this limit in scene-level pruning causes a catastrophic drop in rendering quality. Furthermore, we propose multiple score functions that measure each primitive’s importance in different aspects and degrees, and benchmark their effectiveness. Our extensive experiments show that color similarity with blending weight can most effectively capture important primitives among the proposed score functions.

We summarize our contributions as:

- We classify Gaussian primitive pruning techniques into two categories: scene-level pruning and pixel-level pruning. To the best of our knowledge, this work is the first attempt to categorize these pruning techniques.
- We find that pixel-level pruning method structurally has a boundary of pruning, serving as a built-in limit or safeguard. Additionally, we find that pixel-level pruning is more effective at removing insignificant primitives compared to scene-level pruning.
- We propose multiple variations of score functions based on the rendering equations and conduct extensive experiments. We discover that color similarity and blending

weight together are the most significant factors in discriminating insignificant primitives. In our experiments, the SafeguardGS with the optimal score function shows the highest PSNR-per-primitive performance under an extreme pruning setting, retaining only about 10% of the primitives from the original 3DGS scene (i.e., $10\times$ compression ratio).

2. Related Work

2.1. Efficient neural radiance fields

In recent decades, numerous methods for reconstructing and representing 3D scenes have attracted significant interest in both computer vision and graphics fields. Traditionally, structure-from-motion (SfM) [38] and multi-view stereo (MVS) [13] have been utilized to estimate camera parameters from a collection of images and build dense 3D point representations of object shapes in these images. Subsequently, the streamlined software architecture of SfM and MVS, known as COLMAP [33, 34], has become the de facto practice for generating virtual 3D scenes.

Meanwhile, the groundbreaking approach of NeRF [27], which represents colors and shapes by multi-layer perceptrons (MLPs) encoded features and reconstructs novel view images by synthesizing the features with the volumetric rendering technique, has advanced rendering quality towards photorealism. The success of NeRF has led to its application in various fields, including image processing [6], simultaneous localization and mapping [32, 48], generative modeling [14, 30, 35], and human modeling [4, 12].

Unsurprisingly, among the many challenges in NeRF, such as reconstructing unbounded 3D scenes [46], data sparsity [40, 45], inconsistent data [26], noisy data [25], and temporal data [11, 22], enhancing the efficiency of both rendering and memory has become a significant concern. A notable contribution to efficient NeRF methods is by Sun et al. [39], who identified the bottleneck in MLPs and proposed a hybrid representation combining feature voxel grids with shallow MLPs. Furthermore, Fridovich-Keil et al. [10] achieved faster rendering speeds through completely MLP-less feature grids by employing spherical harmonics (SH). Alternatively, other grid-based methods have proposed using more efficient data structures to avoid the high memory strain from dense grids, such as tensor decomposition [3], hash tables [28], octrees [44], and feature quantization [37]. Although their endeavors have demonstrated rapid scene convergence and improved image quality compared to traditional MLP-based NeRF methods, grid-based methods are not yet deemed perfect due to limitations in bounded image quality imposed by the selection of data structure for grids and hindered forward-pass speed caused by the inherent multiple sampling approach in the volumetric rendering technique.

2.2. Compact 3D scene representation with Gaussian primitives

3D Gaussian Splatting (3DGS) [17] has achieved unprecedented results, establishing a new standard for balancing rendering quality and speed. This remarkable accomplishment is attributed to its MLP-less 3D representation, which utilizes 3D Gaussians to enable real-time, high-quality rendering. Additionally, the explicit 3D scene representation facilitates the use of the typical graphics rendering pipeline, allowing full GPU parallelism.

Despite its state-of-the-art advancement, the densification algorithm of 3DGS [17], which populates new Gaussian primitives in unreconstructed regions, often leads to millions of primitives occupying vast memory space, posing a major new challenge. Initially, the authors [17] addressed this issue by regularly removing primitives with opacity below a manually pre-selected threshold. However, Fan et al. [8] demonstrated that this strategy does not effectively reduce the number of primitives. They showed that an additional 60% pruning, detected through their proposed Gaussian importance evaluation metric, is possible without sacrificing quality. Similarly, concurrent studies have proposed distinct importance metrics to identify unimportant primitives [9, 20, 24, 31, 47]; however, the implications of these methods—particularly the key characteristics to consider when designing such metrics—remain unveiled.

3. Gaussian Primitive Pruning

3.1. Background

3D Gaussian Splatting. 3DGS [17] represents a 3D scene using a set of N 3D Gaussians as geometric primitives. Gaussians $\{\mathbf{G}_i \mid i = 1, 2, 3, \dots, N\}$ are parameterized by center position (mean) $\boldsymbol{\mu}_i \in \mathbb{R}^3$, scale $\mathbf{s}_i \in \mathbb{R}^3$, rotation $\mathbf{r}_i \in \mathbb{R}^4$, opacity $\mathbf{o}_i \in \mathbb{R}$, and k spherical harmonics (SH) coefficients $\mathbf{f}_i \in \mathbb{R}^k$. In practice, the opacity value is activated by a sigmoid function, i.e., $\sigma_i = \sigma(\mathbf{o}_i)$, to bound the range to $[0, 1]$, and the degree of the SH is set to three. Eventually, the total number of parameters of a Gaussian is 59.

In the initialization of the Gaussian primitives, 3DGS uses an SfM-generated sparse point cloud [38] if available, or alternatively, it initializes a fixed number of Gaussians with positions and colors randomly drawn from a uniform distribution. During the first half of training iterations, the densification process is employed to augment the number of primitives, addressing improperly represented geometries (e.g., under-reconstruction and over-reconstruction) and inadequately emerged floaters. After the densification stage, the number of primitives remains constant, and only the remaining primitives are further optimized.

3DGS employs the splatting technique [49, 50] to render images. Each 3D Gaussian with its center $\boldsymbol{\mu}$ is defined as

$G(\mathbf{x}) = \exp(-\frac{1}{2}\mathbf{x}^T\boldsymbol{\Sigma}^{-1}\mathbf{x})$, where the covariance matrix $\boldsymbol{\Sigma}$ in world coordinates is given by $\mathbf{R}\mathbf{S}\mathbf{S}^T\mathbf{R}^T$. Here, \mathbf{R} and \mathbf{S} are the rotation and scale matrices derived from their respective vector forms. Each 3D Gaussian is then projected onto the image plane as a 2D splat \mathcal{G} by omitting the last row and column of the transformed covariance in camera coordinates: $\boldsymbol{\Sigma}' = \mathbf{J}\mathbf{W}\boldsymbol{\Sigma}\mathbf{W}^T\mathbf{J}^T$, where \mathbf{W} is the view transformation matrix, and \mathbf{J} is the Jacobian of the affine-approximated projective transformation. Finally, the color \mathbf{c}_r of each pixel ray $r \in \mathcal{R}$ is determined by progressively accumulating the colors c_i of the projected M splats on the pixel, weighted by w_i , from the nearest to the farthest splats from the camera. Formally,

$$\mathbf{c}_r = \sum_{i \in M} c_i w_i, \quad (1)$$

$$\text{with } w_i = \alpha_i T_i, \quad \alpha_i = \sigma_i \mathcal{G}_i, \quad \text{and } T_i = \prod_{j=1}^{i-1} (1 - \alpha_j).$$

The view-dependent appearance c_i of Gaussian primitive \mathbf{G}_i is computed from its SH coefficients \mathbf{f}_i .

Gaussian primitive pruning. The required model size to represent a 3D scene with Gaussian primitives increases proportionally with the number of primitives. To control the number of primitives, 3DGS introduces the densification process. However, its naive approach of duplicating and removing primitives seems suboptimal and tends to proliferate millions of primitives, as discussed by the authors [17]. For example, a scene represented by one million primitives with full-precision parameters results in a memory pressure of approximately 236MB ($= 59 \times 4\text{Byte} \times 1\text{M}$). Moreover, since the differentiable renderer orders the primitives and accesses them from the nearest to the farthest on a pixel-by-pixel basis, an excessive number of primitives critically hampers rendering speed as well as burdens rendering memory.

Recent works recognize this problem and propose methods to prune primitives based on specific criteria. The common approach involves defining a metric to quantify each primitive’s importance and generating a mask for retaining primitives that meet a specific *pruning setting* (such as pruning ratio, score threshold, or top-k rank) based on the evaluated importance. For instance, LightGaussian [8] defines a global significance score depending on a primitive’s opacity \mathbf{o}_i and adaptively normalized volume $\gamma_i = (\min(\max(\frac{\prod \mathbf{s}_i}{\prod \mathbf{s}_{max,90}}, 0), 1), 1)^{0.1}$, across all training views, and prunes primitives whose importance falls below a pre-selected pruning ratio. Similarly, Mini-Splatting [9] defines an importance score that primarily measures a primitive’s contribution (i.e., w_i in Eq. (1)) to the rendered pixel colors. The number of primitives is controlled by a

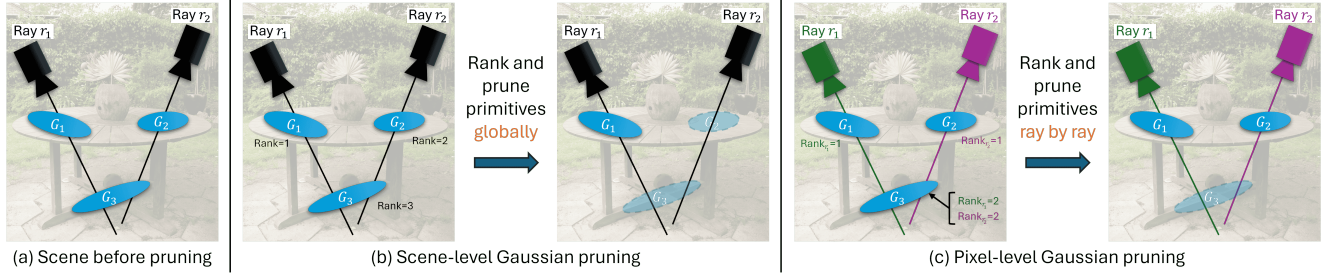


Figure 2. Given a set of Gaussian primitives \mathbf{G}_i (a), scene-level pruning (b) evaluates the importance of each primitive across all rays and orders the primitives globally. Because this pruning is applied at the scene level, some rays may end up rendering nothing afterward. In contrast, pixel-level pruning (c) evaluates each primitive’s contribution and ranks the primitives accordingly independently for each ray, ensuring that primitives are preserved in a way that completely prevents rays from missing intersections with primitives.

predefined pruning ratio, but unlike LightGaussian, Mini-Splatting uses importance scores as the sampling probability for each primitive, and they are stochastically sampled to better maintain overall geometry with the pruning ratio. However, accumulating the importance of each primitive to every pixel may exaggerate importance when a primitive has a high hit count. Meanwhile, RadSplat [31] proposes using the max operator instead of summation and identifies low priority primitives when their maximum contribution across rays falls below a predefined score threshold. Similarly, EfficientGS [24] employs the same idea of measuring primitive’s contribution using blending weight w_i but with a different pruning setting, independently determining the top-k dominant primitives with significant contributions for each pixel and pruning those ranked lower than the predefined k-th rank. The score functions used in these studies are summarized as follows:

$$Score_{LG}(\mathbf{G}_i, \mathcal{R}) = \sum_{r \in \mathcal{R}} \mathbb{1}(\mathbf{G}_i, r) \cdot \sigma_i \cdot \gamma_i, \quad [8]$$

$$Score_{MS}(\mathbf{G}_i, \mathcal{R}) = \sum_{r \in \mathcal{R}} \mathbb{1}(\mathbf{G}_i, r) \cdot w_i, \quad [9]$$

$$Score_{RS}(\mathbf{G}_i, \mathcal{R}) = \max_{r \in \mathcal{R}} \mathbb{1}(\mathbf{G}_i, r) \cdot w_i, \quad [31]$$

$$Score_{EG}(\mathbf{G}_i, r) = w_i. \quad [24]$$

Here, $\mathbb{1}(\mathbf{G}_i, r)$ represents an indicator function that specifies whether the Gaussian primitive \mathbf{G}_i intersects with the ray r or not. $Score(\mathbf{G}_i, \mathcal{R})$ evaluates the contribution of the primitive across all rays \mathcal{R} , while $Score(\mathbf{G}_i, r)$ assesses its contribution with respect to a specific ray r .

3.2. Categorization of Gaussian primitive pruning

We reviewed the contemporary Gaussian primitive pruning efforts in Sec. 3.1. The aforementioned pruning techniques utilize distinct score functions and pruning settings. Essentially, they can be categorized into two types depending on whether the score evaluation considers all rays collectively or each ray independently.

Scene-level pruning. One type of pruning involves evaluating the Gaussian primitives \mathbf{G}_i at a global level [8, 9, 31]. As the term ‘scene-level’ implies, each primitive’s contribution is evaluated across all pixels, either by aggregating or maximizing its impact on the entire scene. The contribution is measured in various ways, with activated opacity σ_i and blending weight w_i being commonly used. Once the scores are computed, primitives that meet a criterion—such as a certain percentage of top-scored primitives, those with scores above a threshold, or the top k-ranked primitives—are retained (Fig. 2 (b)).

Pixel-level pruning. Another type of pruning involves comparing the importance of primitives within the scope of each pixel ray [24]. In this method, a group M of primitives intersecting a ray r is first identified. Each primitive’s contribution to the ray is measured based on its parameters, similar to scene-level pruning. Then, those that meet a defined criterion are marked for retention. This pixel-level masking is repeated for every ray \mathcal{R} . The resulting masks are typically merged using an ‘or’ operation, and primitives are removed based on this final mask (Fig. 2 (c)).

Scene-level vs. pixel-level. The main difference between these two pruning types lies in their scope, which gives pixel-level pruning some unique advantages. Scene-level pruning ranks primitives based on their global importance, which can lead to potential over- or underestimation of importance depending on the number of rays that intersect the primitive. For example, consider a primitive that makes a small, uniform contribution across all rays; its absence would not impact rendering quality. In contrast, consider another primitive that has a high contribution but intersects only a single ray. The Mini-Splatting score function ($Score_{MS}$) might assign a higher score to the first primitive due to its broader exposure, prioritizing it over the second, which could then be pruned. In pixel-level pruning, however, importance is evaluated per ray, allowing the second

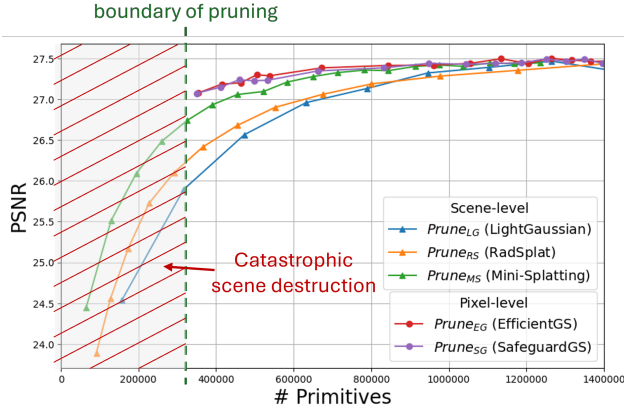


Figure 3. Averaged PSNR over nine scenes from MipNeRF360 [2]. We sweep pruning parameters for each method. Unlike scene-level pruning, pixel-level pruning maintains the number of primitives above a certain boundary, preventing drastic scene degradation while preserving high quality.

primitive to retain its significance to the intersecting ray and increasing the likelihood that the first, less critical primitive will be pruned.

Another advantage of pixel-level pruning is that it guarantees at least one primitive per ray, ensuring every ray renders some content, rather than blank. Intuitively, an extreme pixel-level pruning setting could retain only the highest-contributing primitive for each ray. This provides a natural boundary for pruning since removing any more would result in an empty scene, which is nonsensical. Scene-level pruning, by contrast, lacks such safeguard and carries the risk of leaving some rays with no intersecting primitives if pruning settings are chosen improperly. For instance, if only the top single contributing primitive is kept across the entire scene, many rays may render nothing or only display the same primitive. To avoid this issue, empirically sweeping pruning parameters is essential to find the proper settings with evitable large computing overhead.

To explore the implications of the two types of pruning, we train 3DGS for 30k iterations and apply pruning techniques [8, 9, 24, 31] at 20k iteration, each with sweeping pruning parameters. Fig. 3 shows that the novel view rendering quality according to the number of primitives. We observe that the PSNR value of both pruning types begins to drop at around 0.6 million primitives. However, their slopes differ. While scene-level pruning techniques indiscriminately prune until nothing remained, pixel-level pruning techniques avoid over-decimation of the primitives, maintaining at least around 0.35 million primitives. Moreover, pixel-level pruning always shows better quality compared to scene-level pruning. Apparently, pixel-level pruning prevents inaccurate estimation of importance as well as the catastrophic scene destruction.

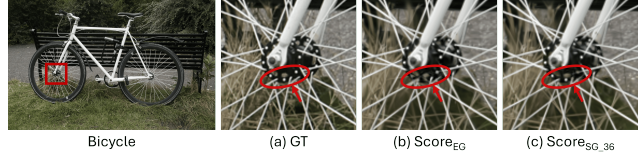


Figure 4. The score function of EfficientGS ($Score_{EG}$) lacks consideration of the colors of Gaussian primitives, resulting in the loss of high-frequency information during pruning, as indicated by the white holes on the wheel axle in (b). Our proposed score function ($Score_{SG_36}$), which is sensitive to the color similarity between the primitive color and the ground truth pixel value, helps preserve the details in (c).

3.3. Importance score functions

Both scene-level pruning and pixel-level pruning techniques require defining a score function assessing the importance of a primitive, as discussed in Sec. 3.1. Furthermore, we have demonstrated in Sec. 3.2 that under aggressive pruning settings, pixel-level pruning can reasonably preserve relatively high quality (EfficientGS with a top-1 criterion in Fig. 3 achieves a PSNR of 27.07 dB with 353k primitives). However, this is still lower compared to 3DGS (PSNR of 27.43 dB). Fig. 4 (a) and (b) compare the rendered image of fully trained 3DGS and the rendered image immediately after pruning by using EfficientGS pruning with a top-1 criterion. This juxtaposition suggests that the score function of EfficientGS is insufficiently sensitive to the color difference between that of primitive and that of the ground truth, resulting in the loss of high-frequency areas when the primitives are pruned too aggressively.

Revisiting the rendering equation, Eq. (1), we notice that the following Gaussian parameters and intermediate values contribute to the rendered color of a pixel: c_i , σ_i , α_i , \mathcal{G}_i , and T_i . Based on these factors, we define various score functions by combining them with appropriate activation of color similarity and pixel closeness, listed as in Tab. 1 (we list part of the proposed score functions here, and please see supplementary material for the full list).

Here, $PC(\cdot, \cdot)$, $CD_1(\cdot, \cdot)$, and $CD_2(\cdot, \cdot)$ are defined functions for pixel closeness and color similarity, specifically:

$$\begin{aligned}
 PC(X_r, X_i) &= \exp(-\|X_r - X_i\|_2), \\
 CS_1(\mathbf{c}_r, c_i) &= (1 - \text{mean}(\|\mathbf{c}_r - c_i\|_1)), \\
 CS_2(\mathbf{c}_r, c_i) &= \exp(-\text{mean}(\|\mathbf{c}_r - c_i\|_1)),
 \end{aligned} \tag{2}$$

where X_r and \mathbf{c}_r are the pixel coordinates and color of the ray r , respectively, and X_i is the center position of the projected splat \mathcal{G}_i .

Through extensive experiments (Sec. 4.2), we discover that $Score_{SG_36}$, which consists of color similarity and blending weight, preserves better high-frequency areas

Table 1. Selected list of proposed score functions

$$Score_{SG.3}(\mathbf{G}_i, r) = \sigma_i * T_i$$

$$Score_{SG.4}(\mathbf{G}_i, r) = \alpha_i * T_i \text{ (equivalent to } Score_{EG})$$

$$Score_{SG.8}(\mathbf{G}_i, r) = PC(X_r, X_i) * \sigma_i * T_i$$

$$Score_{SG.9}(\mathbf{G}_i, r) = PC(X_r, X_i) * \alpha_i * T_i$$

$$Score_{SG.11}(\mathbf{G}_i, r) = \alpha_i + T_i$$

$$Score_{SG.36}(\mathbf{G}_i, r) = CS_1(\mathbf{c}_r, c_i) * \alpha_i * T_i$$

$$Score_{SG.39}(\mathbf{G}_i, r) = CS_1(\mathbf{c}_r, c_i) * PC(X_r, X_i) * \alpha_i$$

$$Score_{SG.40}(\mathbf{G}_i, r) = CS_2(\mathbf{c}_r, c_i) * PC(X_r, X_i) * \sigma * T_i$$

$$Score_{SG.52}(\mathbf{G}_i, r) = CS_2(\mathbf{c}_r, c_i) * \alpha_i * T_i$$

$$Score_{SG.57}(\mathbf{G}_i, r) = CS_2(\mathbf{c}_r, c_i) * PC(X_r, X_i) * \alpha_i + T_i$$

$$Score_{SG.68}(\mathbf{G}_i, r) = CS_1(\mathbf{c}_r, c_i) + \alpha_i * T_i$$

$$Score_{SG.75}(\mathbf{G}_i, r) = CS_1(\mathbf{c}_r, c_i) + \alpha_i + T_i$$

$$Score_{SG.84}(\mathbf{G}_i, r) = CS_2(\mathbf{c}_r, c_i) + \alpha_i * T_i$$

$$Score_{SG.91}(\mathbf{G}_i, r) = CS_2(\mathbf{c}_r, c_i) + \alpha_i + T_i$$

* Refer to Sec. 3.1 and Sec. 3.3 for the meaning of the letters (σ_i , α_i , and T_i) and functions (PC , CS_1 , and CS_2).

compared to $Score_{EG}$, as depicted in Fig. 4 (b) and (c).

3.4. SafeguardGS

We have discussed two key advantages of pixel-level pruning and found that color similarity with blending weight is most effective for scoring primitives. Building on these insights, we propose an optimal pruning technique for 3DGS, called SafeguardGS. SafeguardGS quantifies the significance of each primitive using $Score_{SG.36}$ and prunes according to a top-1 criterion pixel by pixel.

4. Experiment

4.1. Setup

Implementation details. Thanks to the open-source code of 3DGS [17], we readily built our experimental platform. We implemented the primitive pruning algorithm on top of 3DGS’s Python code and extended the CUDA-based differentiable renderer to include the various score functions. We trained each technique for 30k iterations on an NVIDIA A100 GPU. During training, we applied pruning once at 20k iterations for a fair comparison. For other hyperparameters (e.g., learning rates, SH degree scheduling, and densification process), we followed the 3DGS configuration to maintain consistency across all pruning techniques and datasets.

Datasets and Metrics. For the comprehensive comparison of pruning techniques and the effectiveness of importance score functions, we train each pruning technique on various datasets including Synthetic NeRF [27], MipNeRF360 [2], Tanks&Temples [18], and Deep Blending [15], and we evaluate the rendering quality by using PSNR, SSIM, and LPIPS. Additionally, we report the number of

primitives in thousands, the ratio of pruned primitives, and PSNR-per-primitive.

We follow the common approaches for using the datasets. For the Synthetic NeRF dataset, comprising eight small, bounded virtual scenes, we allocate one hundred 800x800 images for training and two hundred 800x800 images for testing. For the unbounded, real-world scenes in the MipNeRF360 dataset (consisting of four indoor scenes and five outdoor scenes), the Tanks&Temples dataset (containing two outdoor scenes), and the Deep Blending dataset (containing two indoor scenes), we use every 8th image for testing and the rest for training at their original resolutions.

Baselines for pruning technique comparison. As our motivation to comprehend the implications of different pruning techniques, we have imported the only the pruning implementations (i.e., pruning setting and score function) from the prior works. The pruning technique notations are $Prune_{LG}$, $Prune_{MS}$, $Prune_{RS}$, $Prune_{EG}$, and $Prune_{SG}$, originating respectively from LightGaussian [8], Mini-Splatting [9], RadSplat [31], and EfficientGS [24], and our proposed method. Note that, as of this paper’s submission, only LightGaussian and Mini-Splatting have open-sourced their codes, so we carefully implemented the pruning techniques for RadSplat and EfficientGS based on the descriptions in their respective papers.

4.2. Study of effective score function

Firstly, we conducted experiments to identify the most effective score function among all proposed ones. For each function proposed in Tab. 1, we swept the top-k criterion from 1 to 100, recording the corresponding reconstruction quality. As expected, higher top-k values allow more primitives to remain, resulting in a larger number of primitives after pruning and thus higher quality. However, the effectiveness of each function varies; some retain primitives that contribute more significantly to reconstruction quality, meaning that a comparable number of primitives yields higher reconstruction fidelity.

In our analysis, we found that the blending weight w_i effectively prioritizes high-quality primitives, positioning curves of $Scor_{SG.4}$ and $Scor_{SG.36}$ at the top in Fig. 5. For further results from additional metrics and datasets, please refer to supplementary material.

To better understand the impact of color similarity, we analyzed the distribution of primitives’ color similarity. Fig. 6 demonstrates that lots of primitives with low color similarity are removed by $Scor_{SG.4}$, while $Scor_{SG.36}$ completely eliminates all primitives with low color similarity. For other scenes, refer to supplementary material.

Tab. 2 displays PSNR-per-primitive across different top-k values, revealing that $Scor_{SG.36}$ effectively prunes thousands of primitives while maintaining nearly the same re-

Table 2. PSNR-per-primitive comparison on MipNeRF360 [2]. The darker the pink color, the better the effectiveness of pruning.

		Top-k														
		1	2	3	4	5	10	20	30	40	50	60	70	80	90	100
$Score_{SG,4}$	PSNR \uparrow	27.074	27.184	27.201	27.298	27.286	27.383	27.413	27.416	27.439	27.495	27.437	27.500	27.479	27.461	27.469
	# Prim. \downarrow (k)	353.134	415.036	463.817	505.024	538.258	671.651	843.440	960.525	1055.747	1133.836	1204.023	1264.763	1316.377	1365.480	1413.110
	PSNR/Prim. \uparrow	7.67E-5	6.55E-5	5.86E-5	5.41E-5	5.07E-5	4.08E-5	3.25E-5	2.85E-5	2.60E-5	2.42E-5	2.28E-5	2.17E-5	2.09E-5	2.01E-5	1.94E-5
$Score_{SG,36}$	PSNR \uparrow	27.073	27.148	27.238	27.225	27.232	27.346	27.384	27.439	27.427	27.438	27.445	27.492	27.462	27.492	27.438
	# Prim. \downarrow (k)	350.294	412.105	459.782	498.216	533.089	662.526	832.465	948.367	1043.723	1120.808	1186.437	1251.024	1303.052	1349.590	1396.247
	PSNR/Prim. \uparrow	7.73E-5	6.59E-5	5.92E-5	5.46E-5	5.11E-5	4.13E-5	3.29E-5	2.89E-5	2.63E-5	2.45E-5	2.31E-5	2.20E-5	2.11E-5	2.04E-5	1.97E-5

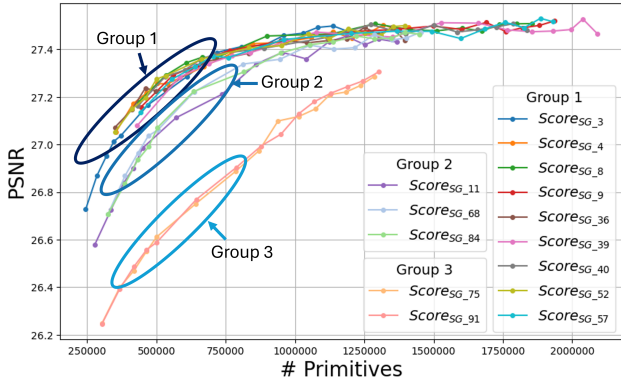


Figure 5. We perform a top-k parameter sweep across a group of proposed score functions, as listed in Tab. 2. Results are averaged over nine scenes from MipNeRF360 [2].

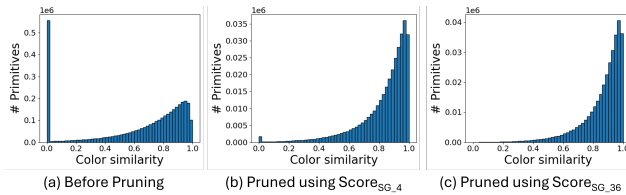


Figure 6. Histograms of color similarity are shown (a) before pruning, (b) after pruning with $Score_{SG,4}$, and (c) with $Score_{SG,36}$. Note that while $Score_{SG,4}$ leaves some invalidated primitives which are having nearly zero color similarity, $Score_{SG,36}$ perfectly prunes them. This graph is collected from the flowers scene in MipNeRF360 [2].

Table 3. Result on Synthetic NeRF [27]. The darker the pink color, the better the effectiveness of pruning.

Prune	PSNR \uparrow	SSIM \uparrow	LPIPS \downarrow	# Prim. \downarrow (k)	Comp. ratio \uparrow	PSNR/Prim. \uparrow
$Prune_{LG}$	31.416	0.9567	0.0490	43.4	85.0%	7.24E-4
$Prune_{MS}$	33.086	0.9666	0.0360	37.1	87.2%	8.93E-4
$Prune_{RS}$	32.787	0.9643	0.0411	38.4	86.7%	8.54E-4
$Prune_{EG}$	32.910	0.9658	0.0369	33.8	88.3%	9.74E-4
$Prune_{SG}$	32.876	0.9657	0.0371	33.8	88.3%	9.73E-4

construction quality as $Score_{SG,4}$. We observed that the PSNR-per-primitive of $Score_{SG,36}$ consistently exceeds that of other functions, concluding that $Score_{SG,36}$ is the optimal choice for effective pruning.

Table 4. Result on MipNeRF360 [2]. The darker the pink color, the better the effectiveness of pruning.

Prune	PSNR \uparrow	SSIM \uparrow	LPIPS \downarrow	# Prim. \downarrow (k)	Comp. ratio \uparrow	PSNR/Prim. \uparrow
$Prune_{LG}$	26.565	0.7794	0.2767	473.1	85.0%	5.62E-5
$Prune_{MS}$	26.929	0.7956	0.2612	389.4	87.7%	6.92E-5
$Prune_{RS}$	26.415	0.7840	0.2833	366.0	88.4%	7.22E-5
$Prune_{EG}$	27.074	0.7889	0.2674	353.1	88.8%	7.67E-5
$Prune_{SG}$	27.073	0.7881	0.2688	350.3	88.9%	7.73E-5

Table 5. Result on TanksAndTemples [18]. The darker the pink color, the better the effectiveness of pruning.

Prune	PSNR \uparrow	SSIM \uparrow	LPIPS \downarrow	# Prim. \downarrow (k)	Comp. ratio \uparrow	PSNR/Prim. \uparrow
$Prune_{LG}$	22.677	0.7889	0.2641	182.2	90.0%	1.24E-4
$Prune_{MS}$	23.127	0.8222	0.2232	191.3	89.5%	1.21E-4
$Prune_{RS}$	22.812	0.8151	0.2395	173.2	90.5%	1.32E-4
$Prune_{EG}$	23.154	0.8188	0.2277	164.8	91.0%	1.41E-4
$Prune_{SG}$	23.060	0.8165	0.2298	162.2	91.1%	1.42E-4

Table 6. Result on Deep Blending [15]. The darker the pink color, the better the effectiveness of pruning.

Prune	PSNR \uparrow	SSIM \uparrow	LPIPS \downarrow	# Prim. \downarrow (k)	Comp. ratio \uparrow	PSNR/Prim. \uparrow
$Prune_{LG}$	29.070	0.8892	0.2781	421.5	85.0%	6.90E-5
$Prune_{MS}$	29.467	0.8987	0.2610	331.9	88.2%	8.88E-5
$Prune_{RS}$	29.305	0.8990	0.2623	307.5	89.0%	9.53E-5
$Prune_{EG}$	29.501	0.8979	0.2627	307.2	89.0%	9.60E-5
$Prune_{SG}$	29.420	0.8973	0.2634	305.0	89.1%	9.65E-5

4.3. Effective pruning technique

We quantitatively compare the effectiveness of contemporary 3DGS pruning techniques. For pixel-level pruning techniques (i.e., $Prune_{EG}$ [24] and $Prune_{SG}$), we select results where the top-k parameter is set to one, compressing the original scene by approximately 90%. To ensure a fair comparison, we select scene-level pruning results that closely match $Prune_{SG}$ in the number of primitives from among the swept pruning parameters.

Results on synthetic scenes, as shown in Tab. 3, indicate that $Prune_{MS}$ outperforms other scene-level pruning techniques. However, the primitive expressiveness metric (PSNR/Prim.) suggests that $Prune_{SG}$ retains more quality-sensitive primitives, with a notably higher value of 0.8E-4. In comparison to $Prune_{EG}$, which results in a sim-

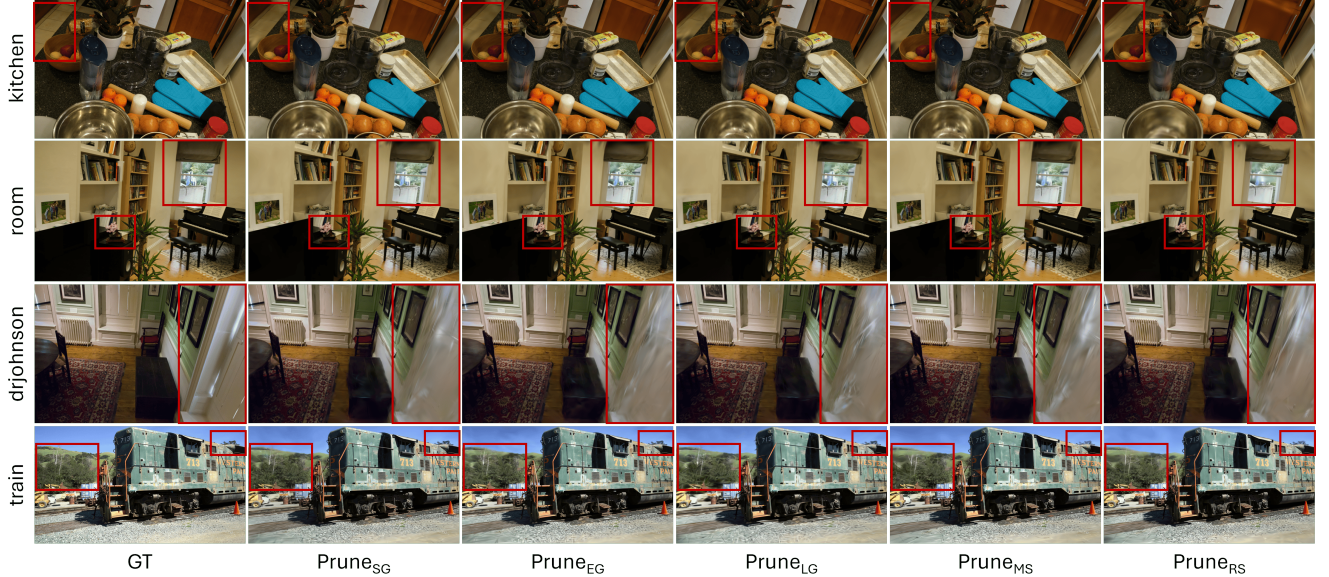


Figure 7. Qualitative result comparison (best viewed in zoom).

ilar number of primitives, $Prune_{SG}$ exhibits only a minor PSNR degradation of 0.034 dB. For real scenes from MipNeRF360 [2], pixel-level pruning techniques achieve higher PSNR despite a reduced number of primitives, outperforming scene-level techniques (Tab. 4). Notably, $Prune_{SG}$ demonstrates the highest primitive expressiveness, advancing $Prune_{EG}$ by $0.06E-5$. Across other real scenes, $Prune_{SG}$ shows minimal quality loss compared to $Prune_{EG}$ due to more aggressive primitive removal, yet it consistently exhibits the highest expressiveness, as seen in Tab. 5 and Tab. 6.

In Fig. 7, we juxtapose rendered images of each pruning technique. Red boxes highlight areas where they have differences, especially retaining primitives closely matching the ground truth pixel colors. For example, in the kitchen scene, other techniques overly prune primitives representing the floor tiles, whereas $Prune_{SG}$ retains them. Similarly, in the drjohnson scene, $Prune_{SG}$ preserves a balanced distribution of primitives across lighted and shaded areas of a door, offering more accurate representation than other techniques.

5. Conclusion

In this paper, we categorize Gaussian primitive pruning techniques and demonstrate that pixel-level pruning, coupled with color similarity with blending weight score function ($Score_{SG,36}$), efficiently works for decimating the primitives with minimal performance degradation. From the experiment comparing the techniques, we observe that while scene-level pruning is prone to destructing the scene unless a careful selection of pruning setting is made, pixel-

level pruning inherently holds a boundary for pruning setting, preventing excessive removal of Gaussian primitives. Moreover, we notice that the importance functions suggested by prior works rarely consider the impact of primitives' colors. We come up with a variety of score function candidates and test them to find the optimal one. We confirm that the pixel-level pruning technique, using the optimal score function ($Score_{SG,36}$), achieves state-of-the-art efficiency by maximizing primitive expressiveness, reducing training time, and increasing FPS, all with an impressive 90% compression ratio. We believe our work provides valuable insights for selecting an effective pruning method for future studies.

Limitation We mainly focus on pruning effectiveness in this paper. While our study achieves state-of-the-art pruning effectiveness with a 90% compression ratio and provides a safeguard against catastrophic scene degradation, the rendering quality is slightly worse than that of 3DGS. Moreover, pruning the primitives after the densification stage scarcely helps reduce peak memory usage. We observe that incorporating the proposed pruning technique during the densification stage results in significantly faster training speeds with imperceptible performance drops on the Synthetic NeRF dataset. However, this is not the case for unbounded real-world scenes. Furthermore, like 3DGS, our method does not handle scenes containing various appearances across the training images. Lastly, our method greatly depends on the size of the training data (the total number of pixels of all training images).

Acknowledgments

Supported by the Intelligence Advanced Research Projects Activity (IARPA) via Department of Interior/ Interior Business Center (DOI/IBC) contract number 140D0423C0076. The U.S. Government is authorized to reproduce and distribute reprints for Governmental purposes notwithstanding any copyright annotation thereon. Disclaimer: The views and conclusions contained herein are those of the authors and should not be interpreted as necessarily representing the official policies or endorsements, either expressed or implied, of IARPA, DOI/IBC, or the U.S. Government.

References

- [1] Jonathan T Barron, Ben Mildenhall, Matthew Tancik, Peter Hedman, Ricardo Martin-Brualla, and Pratul P Srinivasan. Mip-nerf: A multiscale representation for anti-aliasing neural radiance fields. In *Proceedings of the IEEE/CVF International Conference on Computer Vision*, pages 5855–5864, 2021. 1
- [2] Jonathan T Barron, Ben Mildenhall, Dor Verbin, Pratul P Srinivasan, and Peter Hedman. Mip-nerf 360: Unbounded anti-aliased neural radiance fields. In *Proceedings of the IEEE/CVF Conference on Computer Vision and Pattern Recognition*, pages 5470–5479, 2022. 1, 5, 6, 7, 8, 2, 3
- [3] Anpei Chen, Zexiang Xu, Andreas Geiger, Jingyi Yu, and Hao Su. Tensorf: Tensorial radiance fields. In *European Conference on Computer Vision*, pages 333–350. Springer, 2022. 1, 2
- [4] Mingfei Chen, Jianfeng Zhang, Xiangyu Xu, Lijuan Liu, Yujun Cai, Jiashi Feng, and Shuicheng Yan. Geometry-guided progressive nerf for generalizable and efficient neural human rendering. In *European Conference on Computer Vision*, pages 222–239. Springer, 2022. 2
- [5] Zhiqin Chen, Thomas Funkhouser, Peter Hedman, and Andrea Tagliasacchi. Mobilenerf: Exploiting the polygon rasterization pipeline for efficient neural field rendering on mobile architectures. In *Proceedings of the IEEE/CVF Conference on Computer Vision and Pattern Recognition*, pages 16569–16578, 2023. 1
- [6] Mikolaj Czerkawski, Javier Cardona, Robert Atkinson, Craig Michie, Ivan Andonovic, Carmine Clemente, and Christos Tachtatzis. Neural knitworks: Patched neural implicit representation networks. *Pattern Recognition*, page 110378, 2024. 2
- [7] Nianchen Deng, Zhenyi He, Jiannan Ye, Budmonde Duinkharjav, Praneeth Chakravarthula, Xubo Yang, and Qi Sun. Fov-nerf: Foveated neural radiance fields for virtual reality. *IEEE Transactions on Visualization and Computer Graphics*, 28(11):3854–3864, 2022. 1
- [8] Zhiwen Fan, Kevin Wang, Kairun Wen, Zehao Zhu, De-jia Xu, and Zhangyang Wang. Lightgaussian: Unbounded 3d gaussian compression with 15x reduction and 200+ fps. *arXiv preprint arXiv:2311.17245*, 2023. 1, 3, 4, 5, 6, 2
- [9] Guangchi Fang and Bing Wang. Mini-Splatting: Representing Scenes with a Constrained Number of Gaussians, 2024. 1, 3, 4, 5, 6, 2
- [10] Sara Fridovich-Keil, Alex Yu, Matthew Tancik, Qinhong Chen, Benjamin Recht, and Angjoo Kanazawa. Plenoxels: Radiance fields without neural networks. In *Proceedings of the IEEE/CVF Conference on Computer Vision and Pattern Recognition*, pages 5501–5510, 2022. 1, 2
- [11] Chen Gao, Ayush Saraf, Johannes Kopf, and Jia-Bin Huang. Dynamic view synthesis from dynamic monocular video. In *Proceedings of the IEEE/CVF International Conference on Computer Vision*, pages 5712–5721, 2021. 2
- [12] Xiangjun Gao, Jiaolong Yang, Jongyoo Kim, Sida Peng, Zicheng Liu, and Xin Tong. Mps-nerf: Generalizable 3d human rendering from multiview images. *IEEE Transactions on Pattern Analysis and Machine Intelligence*, 2022. 2
- [13] Michael Goesele, Noah Snavely, Brian Curless, Hugues Hoppe, and Steven M Seitz. Multi-view stereo for community photo collections. In *2007 IEEE 11th International Conference on Computer Vision*, pages 1–8. IEEE, 2007. 2
- [14] Jiatao Gu, Lingjie Liu, Peng Wang, and Christian Theobalt. Stylenerf: A style-based 3d-aware generator for high-resolution image synthesis. *arXiv preprint arXiv:2110.08985*, 2021. 2
- [15] Peter Hedman, Julien Philip, True Price, Jan-Michael Frahm, George Drettakis, and Gabriel Brostow. Deep blending for free-viewpoint image-based rendering. *ACM Transactions on Graphics (ToG)*, 37(6):1–15, 2018. 6, 7, 1, 2, 3, 8
- [16] Peter Hedman, Pratul P Srinivasan, Ben Mildenhall, Jonathan T Barron, and Paul Debevec. Baking neural radiance fields for real-time view synthesis. In *Proceedings of the IEEE/CVF International Conference on Computer Vision*, pages 5875–5884, 2021. 1
- [17] Bernhard Kerbl, Georgios Kopanas, Thomas Leimkühler, and George Drettakis. 3d gaussian splatting for real-time radiance field rendering. *ACM Transactions on Graphics*, 42(4):1–14, 2023. 1, 3, 6
- [18] Arno Knapitsch, Jaesik Park, Qian-Yi Zhou, and Vladlen Koltun. Tanks and temples: Benchmarking large-scale scene reconstruction. *ACM Transactions on Graphics (ToG)*, 36(4):1–13, 2017. 6, 7, 1, 2, 3, 8
- [19] Andreas Kurz, Thomas Neff, Zhaoyang Lv, Michael Zollhöfer, and Markus Steinberger. Adanerf: Adaptive sampling for real-time rendering of neural radiance fields. In *Computer Vision – ECCV 2022*, pages 254–270, Cham, 2022. Springer Nature Switzerland. 1
- [20] Joo Chan Lee, Daniel Rho, Xiangyu Sun, Jong Hwan Ko, and Eunbyung Park. Compact 3D Gaussian Representation for Radiance Field, 2024. 1, 3
- [21] Ruilong Li, Hang Gao, Matthew Tancik, and Angjoo Kanazawa. Nerfacc: Efficient sampling accelerates nerfs. In *Proceedings of the IEEE/CVF International Conference on Computer Vision*, pages 18537–18546, 2023. 1
- [22] Zhengqi Li, Simon Niklaus, Noah Snavely, and Oliver Wang. Neural scene flow fields for space-time view synthesis of dynamic scenes. In *Proceedings of the IEEE/CVF Conference on Computer Vision and Pattern Recognition*, pages 6498–6508, 2021. 2
- [23] Zhaoshuo Li, Thomas Müller, Alex Evans, Russell H Taylor, Mathias Unberath, Ming-Yu Liu, and Chen-Hsuan Lin.

- Neuralangelo: High-fidelity neural surface reconstruction. In *IEEE Conference on Computer Vision and Pattern Recognition (CVPR)*, 2023. 1
- [24] Wenkai Liu, Tao Guan, Bin Zhu, Lili Ju, Zikai Song, Dan Li, Yuesong Wang, and Wei Yang. Efficientgs: Streamlining gaussian splatting for large-scale high-resolution scene representation. *arXiv preprint arXiv:2404.12777*, 2024. 1, 3, 4, 5, 6, 7, 2
- [25] Li Ma, Xiaoyu Li, Jing Liao, Qi Zhang, Xuan Wang, Jue Wang, and Pedro V Sander. Deblur-nerf: Neural radiance fields from blurry images. In *Proceedings of the IEEE/CVF Conference on Computer Vision and Pattern Recognition*, pages 12861–12870, 2022. 2
- [26] Ricardo Martin-Brualla, Noha Radwan, Mehdi SM Sajjadi, Jonathan T Barron, Alexey Dosovitskiy, and Daniel Duckworth. Nerf in the wild: Neural radiance fields for unconstrained photo collections. In *Proceedings of the IEEE/CVF Conference on Computer Vision and Pattern Recognition*, pages 7210–7219, 2021. 2
- [27] Ben Mildenhall, Pratul P. Srinivasan, Matthew Tancik, Jonathan T. Barron, Ravi Ramamoorthi, and Ren Ng. Nerf: Representing scenes as neural radiance fields for view synthesis. In *ECCV*, 2020. 1, 2, 6, 7, 3, 4
- [28] Thomas Müller, Alex Evans, Christoph Schied, and Alexander Keller. Instant neural graphics primitives with a multiresolution hash encoding. *ACM transactions on graphics (TOG)*, 41(4):1–15, 2022. 1, 2
- [29] Thomas Neff, Pascal Stadlbauer, Mathias Parger, Andreas Kurz, Joerg H Mueller, Chakravarty R Alla Chaitanya, Anton Kaplanyan, and Markus Steinberger. Donerf: Towards real-time rendering of compact neural radiance fields using depth oracle networks. In *Computer Graphics Forum*, pages 45–59. Wiley Online Library, 2021. 1
- [30] Michael Niemeyer and Andreas Geiger. Giraffe: Representing scenes as compositional generative neural feature fields. In *Proceedings of the IEEE/CVF Conference on Computer Vision and Pattern Recognition*, pages 11453–11464, 2021. 2
- [31] Michael Niemeyer, Fabian Manhardt, Marie-Julie Rakotosaona, Michael Oechsle, Daniel Duckworth, Rama Gosula, Keisuke Tateno, John Bates, Dominik Kaeser, and Federico Tombari. RadSplat: Radiance Field-Informed Gaussian Splatting for Robust Real-Time Rendering with 900+ FPS, 2024. 1, 2, 3, 4, 5, 6
- [32] Antoni Rosinol, John J Leonard, and Luca Carlone. Nerfslam: Real-time dense monocular slam with neural radiance fields. In *2023 IEEE/RSJ International Conference on Intelligent Robots and Systems (IROS)*, pages 3437–3444. IEEE, 2023. 1, 2
- [33] Johannes Lutz Schönberger and Jan-Michael Frahm. Structure-from-Motion Revisited. In *Conference on Computer Vision and Pattern Recognition (CVPR)*, 2016. 2
- [34] Johannes Lutz Schönberger, Enliang Zheng, Marc Pollefeys, and Jan-Michael Frahm. Pixelwise View Selection for Unstructured Multi-View Stereo. In *European Conference on Computer Vision (ECCV)*, 2016. 2
- [35] Katja Schwarz, Yiyi Liao, Michael Niemeyer, and Andreas Geiger. Graf: Generative radiance fields for 3d-aware image synthesis. *Advances in Neural Information Processing Systems*, 33:20154–20166, 2020. 2
- [36] Chuanyue Shen, Letian Zhang, Zhangsihao Yang, Masood Mortazavi, Xiyun Song, Liang Peng, and Heather Yu. Envisioning a next generation extended reality conferencing system with efficient photorealistic human rendering. In *Proceedings of the IEEE/CVF Conference on Computer Vision and Pattern Recognition*, pages 4622–4631, 2023. 1
- [37] Seungjoo Shin and Jaesik Park. Binary radiance fields. *Advances in Neural Information Processing Systems*, 36, 2024. 2
- [38] Noah Snavely, Steven M Seitz, and Richard Szeliski. Photo tourism: exploring photo collections in 3d. In *ACM siggraph 2006 papers*, pages 835–846. 2006. 2, 3
- [39] Cheng Sun, Min Sun, and Hwann-Tzong Chen. Direct voxel grid optimization: Super-fast convergence for radiance fields reconstruction. In *Proceedings of the IEEE/CVF Conference on Computer Vision and Pattern Recognition*, pages 5459–5469, 2022. 2
- [40] Qianqian Wang, Zhicheng Wang, Kyle Genova, Pratul P Srinivasan, Howard Zhou, Jonathan T Barron, Ricardo Martin-Brualla, Noah Snavely, and Thomas Funkhouser. Ibrnet: Learning multi-view image-based rendering. In *Proceedings of the IEEE/CVF Conference on Computer Vision and Pattern Recognition*, pages 4690–4699, 2021. 2
- [41] Yiming Wang, Qin Han, Marc Habermann, Kostas Daniilidis, Christian Theobalt, and Lingjie Liu. Neus2: Fast learning of neural implicit surfaces for multi-view reconstruction. In *Proceedings of the IEEE/CVF International Conference on Computer Vision*, pages 3295–3306, 2023. 1
- [42] Christopher Xie, Keunhong Park, Ricardo Martin-Brualla, and Matthew Brown. Fig-nerf: Figure-ground neural radiance fields for 3d object category modelling. In *2021 International Conference on 3D Vision (3DV)*, pages 962–971. IEEE, 2021. 1
- [43] Lin Yen-Chen, Pete Florence, Jonathan T Barron, Alberto Rodriguez, Phillip Isola, and Tsung-Yi Lin. inerf: Inverting neural radiance fields for pose estimation. In *2021 IEEE/RSJ International Conference on Intelligent Robots and Systems (IROS)*, pages 1323–1330. IEEE, 2021. 1
- [44] Alex Yu, Ruilong Li, Matthew Tancik, Hao Li, Ren Ng, and Angjoo Kanazawa. Plenotrees for real-time rendering of neural radiance fields. In *Proceedings of the IEEE/CVF International Conference on Computer Vision*, pages 5752–5761, 2021. 1, 2
- [45] Alex Yu, Vickie Ye, Matthew Tancik, and Angjoo Kanazawa. pixelnerf: Neural radiance fields from one or few images. In *Proceedings of the IEEE/CVF Conference on Computer Vision and Pattern Recognition*, pages 4578–4587, 2021. 2
- [46] Kai Zhang, Gernot Riegler, Noah Snavely, and Vladlen Koltun. Nerf++: Analyzing and improving neural radiance fields. *arXiv preprint arXiv:2010.07492*, 2020. 2
- [47] Zhaoliang Zhang, Tianchen Song, Yongjae Lee, Li Yang, Cheng Peng, Rama Chellappa, and Deliang Fan. Lp-3dgs: Learning to prune 3d gaussian splatting, 2024. 3
- [48] Zihan Zhu, Songyou Peng, Viktor Larsson, Zhaopeng Cui, Martin R Oswald, Andreas Geiger, and Marc Pollefeys.

Nicer-slam: Neural implicit scene encoding for rgb slam.
arXiv preprint arXiv:2302.03594, 2023. [1](#), [2](#)

- [49] Matthias Zwicker, Hanspeter Pfister, Jeroen Van Baar, and Markus Gross. Ewa volume splatting. In *Proceedings Visualization, 2001. VIS'01.*, pages 29–538. IEEE, 2001. [1](#), [3](#)
- [50] Matthias Zwicker, Hanspeter Pfister, Jeroen van Baar, and Markus Gross. Surface splatting. In *Proceedings of the 28th Annual Conference on Computer Graphics and Interactive Techniques*, page 371–378, New York, NY, USA, 2001. Association for Computing Machinery. [1](#), [3](#)

SafeguardGS: 3D Gaussian Primitive Pruning While Avoiding Catastrophic Scene Destruction

Supplementary Material

6. Score functions

The rendering equation Eq. (1) gives good hints for scoring the importance of Gaussian primitives since it directly relates to pixel colors. From the factors and intermediate values of Eq. (1) (i.e., $c_i, \sigma_i, \alpha_i, \mathcal{G}_i, T_i$), we design multiple candidates of effective score function. Because of $\alpha_i = \sigma_i \mathcal{G}_i$, rather than we use directly \mathcal{G}_i , we choose the distance between the center of \mathcal{G}_i and pixel position. Furthermore, to ensure the factors doesn't dominate in the score calculation, we properly map (squash) their values into $[0, 1]$ by using L1-norm, L2-norm, and cosine similarity function. The squashing functions are:

$$\begin{aligned} PC(X_r, X_i) &= \exp(-\|X_r - X_i\|_2), \\ CS_1(\mathbf{c}_r, c_i) &= (1 - \text{mean}(\|\mathbf{c}_r - c_i\|_1)), \\ CS_2(\mathbf{c}_r, c_i) &= \exp(-\text{mean}(\|\mathbf{c}_r - c_i\|_1)), \\ CS_3(\mathbf{c}_r, c_i) &= (\mathbf{c}_r \cdot c_i) / (\|\mathbf{c}_r\|_2 * \|c_i\|_2), \end{aligned}$$

where X_r and \mathbf{c}_r are, respectively, the pixel coordinates and color of the ray r , X_i is center of \mathcal{G}_i , \cdot is vector inner product, and $*$ is scalar multiplication.

Tab. 7 lists the full set of functions. Note that the number *id* in the function name $Score_{SG.id}$ is nothing but the score function id.

7. Preliminary Search of Effective Score Function Candidates

Given the full set of functions from Tab. 7, we performed a pilot study to reduce the number of candidates for the top-k parameter sweep experiment. In the pilot study, we selected two datasets (i.e., Synthetic NeRF [27] and MipNeRF360 [2]), as shown in Figs. 8 and 9. We trained 3DGS for 30k iterations and performed pruning once at 20k with the top-1 setting for each score function. Other hyperparameters were kept the same as in the vanilla 3DGS. To make the plot legible, we divided the points into two groups. Based on $Score_{SG.3}$ and $Score_{SG.4}$, we narrowed down the candidates, resulting in Tab. 2.

We further present the top-k parameter sweep results in terms of PSNR, SSIM, and LPIPS metrics across four datasets: Synthetic NeRF [27], MipNeRF360 [2], TanksAndTemples [18], and Deep Blending [15], as shown in Figs. 10 to 13.

Table 7. The full list of score functions

$Score_{SG.1}(\mathbf{G}_i, r) = \sigma_i$
$Score_{SG.2}(\mathbf{G}_i, r) = \alpha_i$
$Score_{SG.3}(\mathbf{G}_i, r) = \sigma_i * T_i$
$Score_{SG.4}(\mathbf{G}_i, r) = \alpha_i * T_i$
$Score_{SG.5}(\mathbf{G}_i, r) = PC(X_r, X_i)$
$Score_{SG.6}(\mathbf{G}_i, r) = PC(X_r, X_i) * \sigma_i$
$Score_{SG.7}(\mathbf{G}_i, r) = PC(X_r, X_i) * \alpha_i$
$Score_{SG.8}(\mathbf{G}_i, r) = PC(X_r, X_i) * \sigma_i * T_i$
$Score_{SG.9}(\mathbf{G}_i, r) = PC(X_r, X_i) * \alpha_i * T_i$
$Score_{SG.11}(\mathbf{G}_i, r) = \alpha_i + T_i$
$Score_{SG.16}(\mathbf{G}_i, r) = CS_3(\mathbf{G}_i, r)$
$Score_{SG.17}(\mathbf{G}_i, r) = CS_3(\mathbf{G}_i, r) * \sigma_i$
$Score_{SG.18}(\mathbf{G}_i, r) = CS_3(\mathbf{G}_i, r) * \alpha_i$
$Score_{SG.19}(\mathbf{G}_i, r) = CS_3(\mathbf{G}_i, r) * \sigma_i * T_i$
$Score_{SG.20}(\mathbf{G}_i, r) = CS_3(\mathbf{G}_i, r) * \alpha_i * T_i$
$Score_{SG.21}(\mathbf{G}_i, r) = CS_3(\mathbf{G}_i, r) * PC(X_r, X_i)$
$Score_{SG.22}(\mathbf{G}_i, r) = CS_3(\mathbf{G}_i, r) * PC(X_r, X_i) * \sigma_i$
$Score_{SG.23}(\mathbf{G}_i, r) = CS_3(\mathbf{G}_i, r) * PC(X_r, X_i) * \alpha_i$
$Score_{SG.24}(\mathbf{G}_i, r) = CS_3(\mathbf{G}_i, r) * PC(X_r, X_i) * \sigma_i * T_i$
$Score_{SG.25}(\mathbf{G}_i, r) = CS_3(\mathbf{G}_i, r) * PC(X_r, X_i) * \alpha_i * T_i$
$Score_{SG.32}(\mathbf{G}_i, r) = CS_1(\mathbf{G}_i, r)$
$Score_{SG.33}(\mathbf{G}_i, r) = CS_1(\mathbf{G}_i, r) * \sigma_i$
$Score_{SG.34}(\mathbf{G}_i, r) = CS_1(\mathbf{G}_i, r) * \alpha_i$
$Score_{SG.35}(\mathbf{G}_i, r) = CS_1(\mathbf{G}_i, r) * \sigma_i * T_i$
$Score_{SG.36}(\mathbf{G}_i, r) = CS_1(\mathbf{G}_i, r) * \alpha_i * T_i$
$Score_{SG.37}(\mathbf{G}_i, r) = CS_1(\mathbf{G}_i, r) * PC(X_r, X_i)$
$Score_{SG.38}(\mathbf{G}_i, r) = CS_1(\mathbf{G}_i, r) * PC(X_r, X_i) * \sigma_i$
$Score_{SG.39}(\mathbf{G}_i, r) = CS_1(\mathbf{G}_i, r) * PC(X_r, X_i) * \alpha_i$
$Score_{SG.40}(\mathbf{G}_i, r) = CS_1(\mathbf{G}_i, r) * PC(X_r, X_i) * \sigma_i * T_i$
$Score_{SG.41}(\mathbf{G}_i, r) = CS_1(\mathbf{G}_i, r) * PC(X_r, X_i) * \alpha_i * T_i$
$Score_{SG.48}(\mathbf{G}_i, r) = CS_2(\mathbf{G}_i, r)$
$Score_{SG.49}(\mathbf{G}_i, r) = CS_2(\mathbf{G}_i, r) * \sigma_i$
$Score_{SG.50}(\mathbf{G}_i, r) = CS_2(\mathbf{G}_i, r) * \alpha_i$
$Score_{SG.51}(\mathbf{G}_i, r) = CS_2(\mathbf{G}_i, r) * \sigma_i * T_i$
$Score_{SG.52}(\mathbf{G}_i, r) = CS_2(\mathbf{G}_i, r) * \alpha_i * T_i$
$Score_{SG.53}(\mathbf{G}_i, r) = CS_2(\mathbf{G}_i, r) * PC(X_r, X_i)$
$Score_{SG.54}(\mathbf{G}_i, r) = CS_2(\mathbf{G}_i, r) * PC(X_r, X_i) * \sigma_i$
$Score_{SG.55}(\mathbf{G}_i, r) = CS_2(\mathbf{G}_i, r) * PC(X_r, X_i) * \alpha_i$
$Score_{SG.56}(\mathbf{G}_i, r) = CS_2(\mathbf{G}_i, r) * PC(X_r, X_i) * \sigma_i * T_i$
$Score_{SG.57}(\mathbf{G}_i, r) = CS_2(\mathbf{G}_i, r) * PC(X_r, X_i) * \alpha_i * T_i$
$Score_{SG.68}(\mathbf{G}_i, r) = CS_1(\mathbf{G}_i, r) + \alpha_i * T_i$
$Score_{SG.75}(\mathbf{G}_i, r) = CS_1(\mathbf{G}_i, r) + \alpha_i + T_i$
$Score_{SG.84}(\mathbf{G}_i, r) = CS_2(\mathbf{G}_i, r) + \alpha_i * T_i$
$Score_{SG.91}(\mathbf{G}_i, r) = CS_2(\mathbf{G}_i, r) + \alpha_i + T_i$

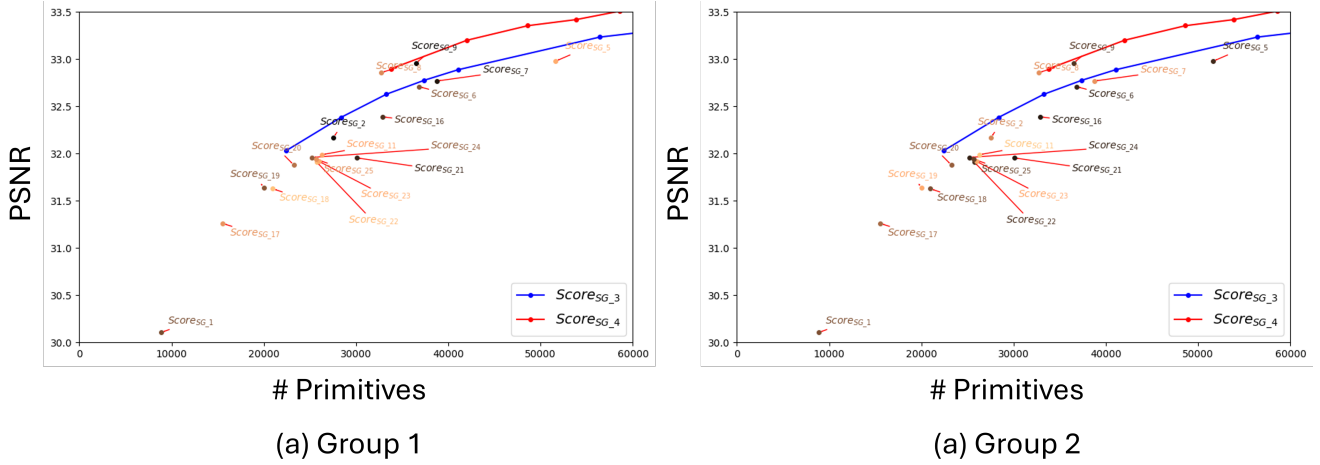


Figure 8. PSNR vs. #Primitives plot for the top-1 setting of score functions in Tab. 7. The PSNR values are averaged across 8 scenes from Synthetic NeRF [27]. For clarity, the dots are plotted separately in group 1 (a) and group 2 (b).

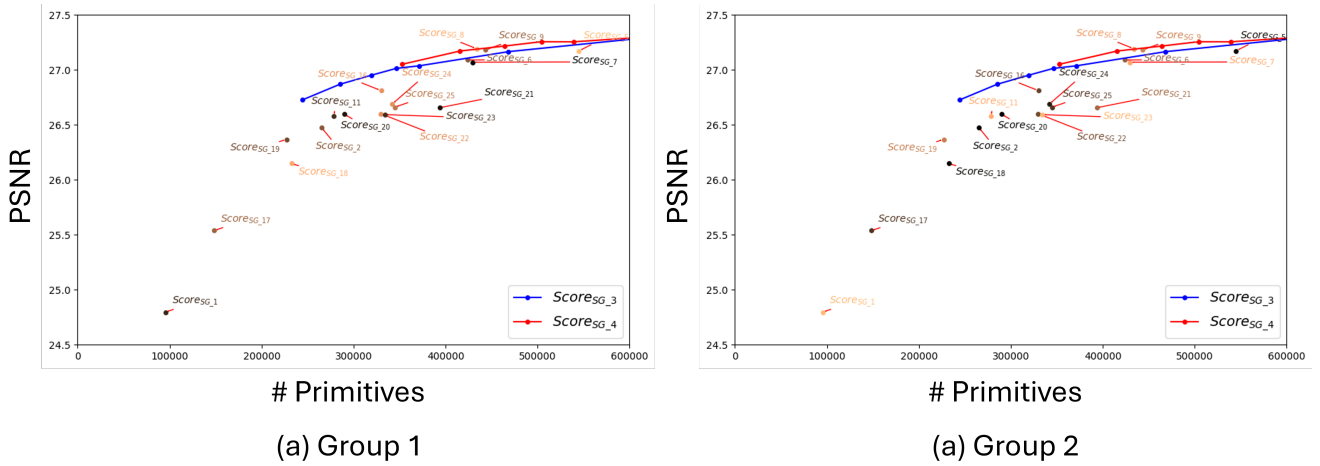


Figure 9. PSNR vs. #Primitives plot for the top-1 setting of score functions in Tab. 7. The PSNR values are averaged across 9 scenes from MipNeRF360 [2]. For clarity, the dots are plotted separately in group 1 (a) and group 2 (b).

8. Color Similarity Distribution of Primitives

Across all scenes, we consistently observe that the color similarity distribution is pushed toward 1, as marked by the lower 1% of primitives’ color similarity values through Figs. 14 to 17. Moreover, we observe that the number of primitives remaining after pruning with $Score_{SG-36}$ is generally smaller than that with $Score_{SG-4}$. This phenomenon implies that $Score_{SG-36}$ more effectively selects primitives crucial for maintaining scene rendering quality.

9. Rendering Result

Through Figs. 18 to 20, we present selected rendered images for each scene from MipNeRF360 [2], TanksAndTemples [18], and Deep Blending [15] to illustrate the visual

quality of pruned scenes using SafeguardGS and baseline methods [8, 9, 24, 31].

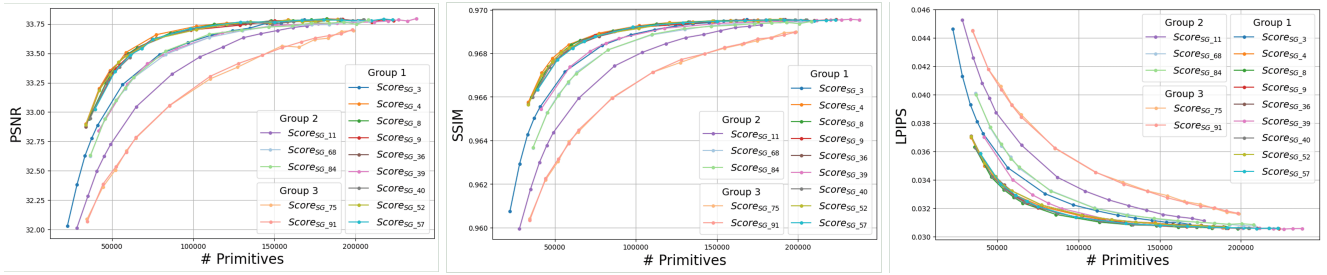


Figure 10. Sweep on the top-k parameter of the selected functions in Tab. 2. The values are averaged over 8 scenes from Synthetic NeRF [27].

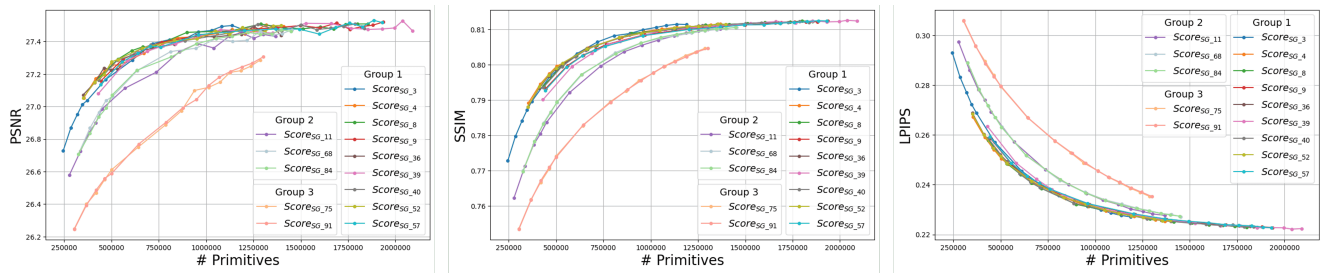


Figure 11. Sweep on the top-k parameter of the selected functions in Tab. 2. The values are averaged over 9 scenes from MipNeRF360 [2].

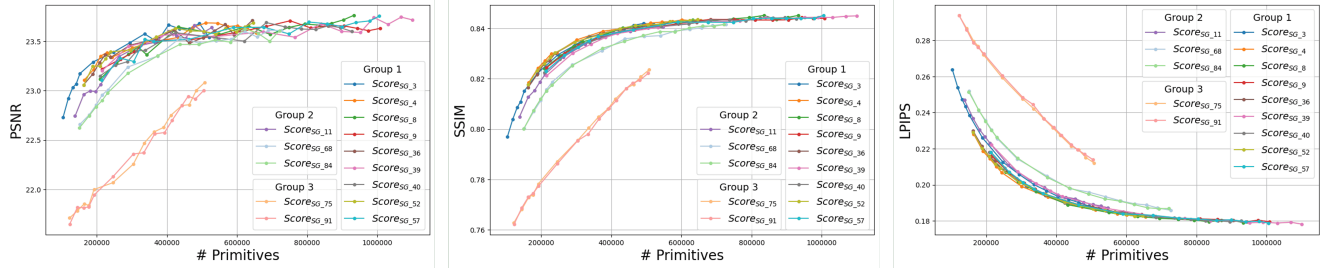


Figure 12. Sweep on the top-k parameter of the selected functions in Tab. 2. The values are averaged over 2 scenes from TanksAndTemples [18].

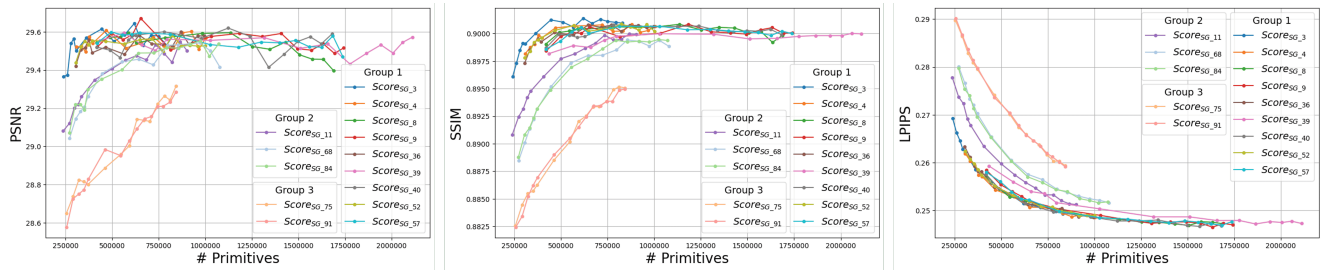


Figure 13. Sweep on the top-k parameter of the selected functions in Tab. 2. The values are averaged over 2 scenes from Deep Blending [15].

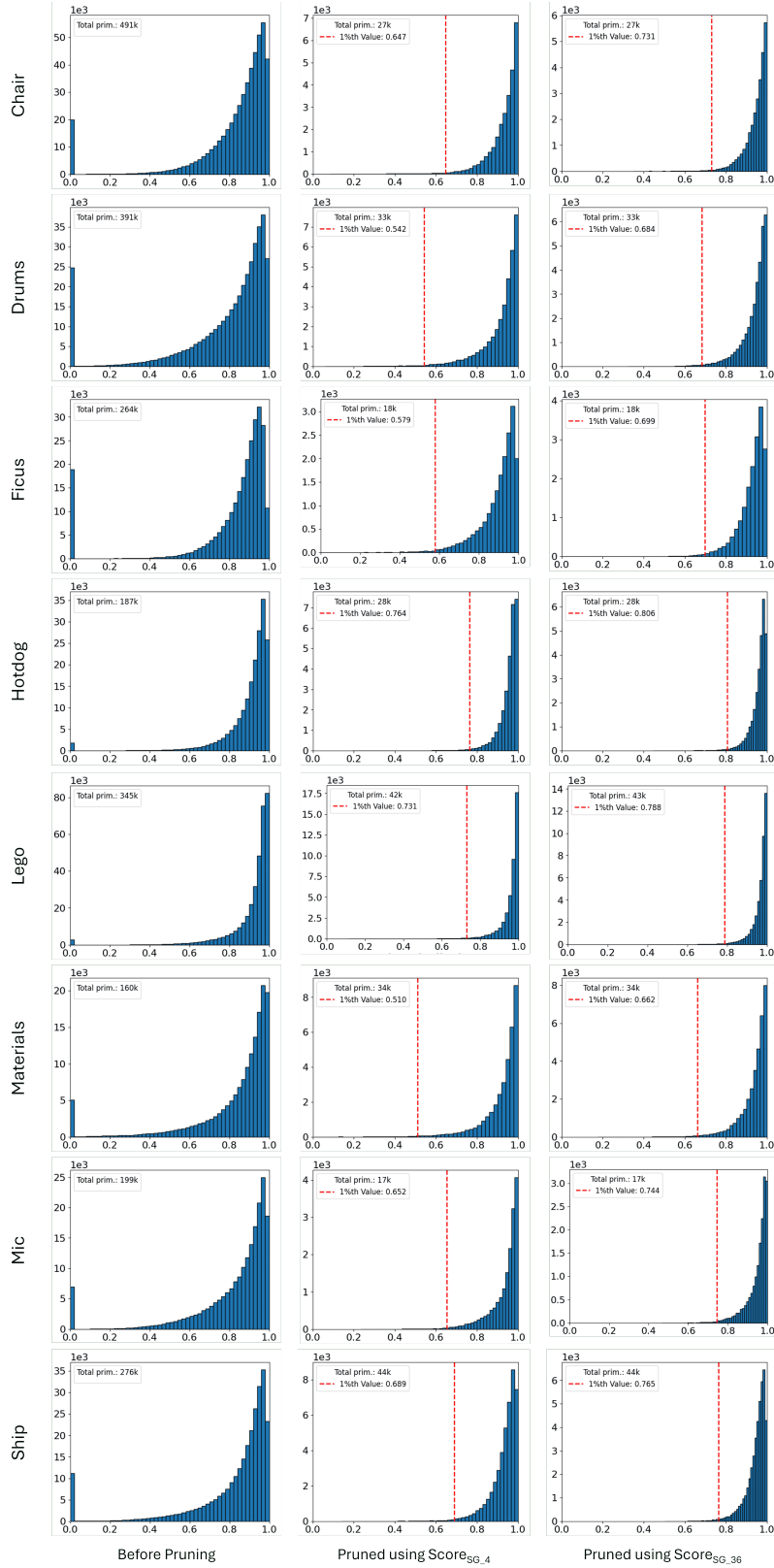


Figure 14. Histogram of primitives' color similarity across 8 scenes from Synthetic NeRF [27]. The X-axis represents color similarity, and the Y-axis shows the number of primitives associated into each bin.

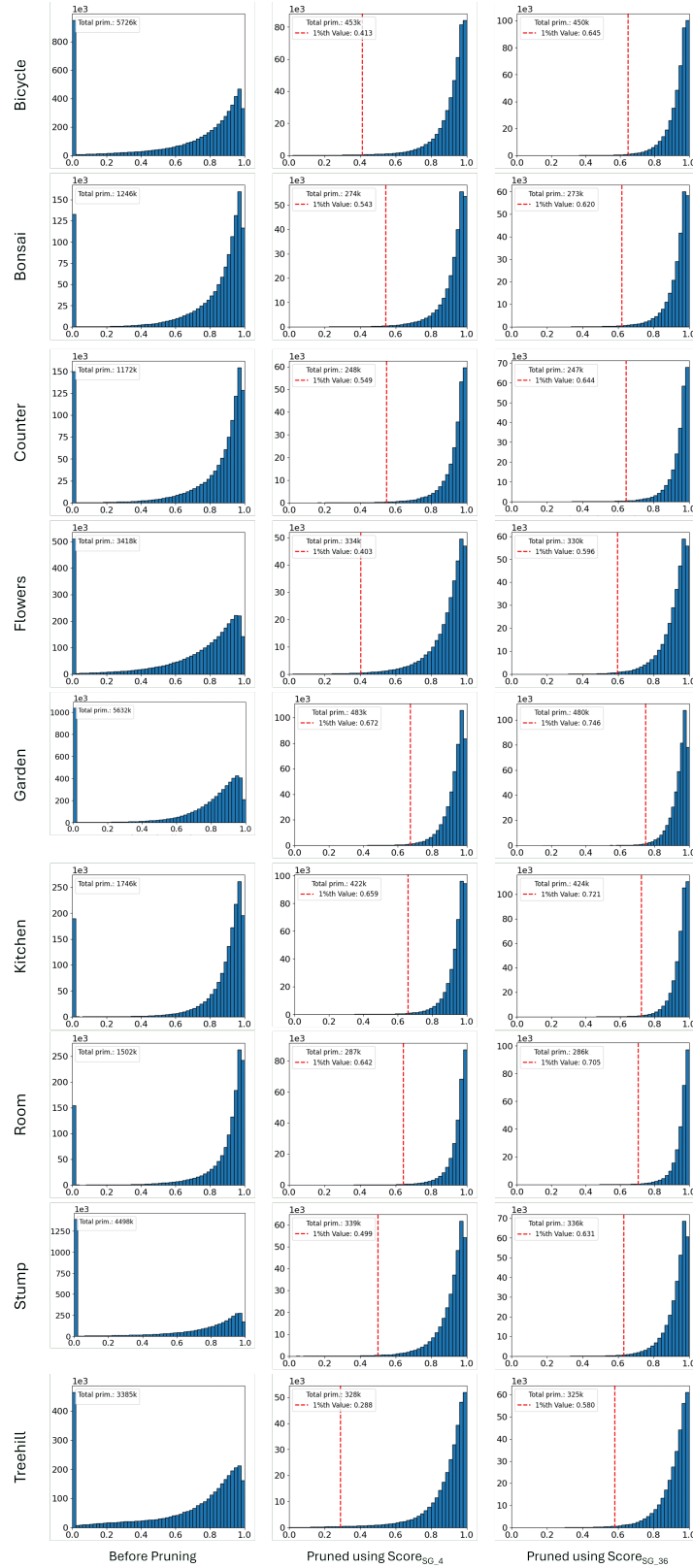


Figure 15. Histogram of primitive’s color similarity over 9 scenes from MipNeRF360 [2]. The X-axis represents color similarity, and the Y-axis shows the number of primitives associated into each bin.

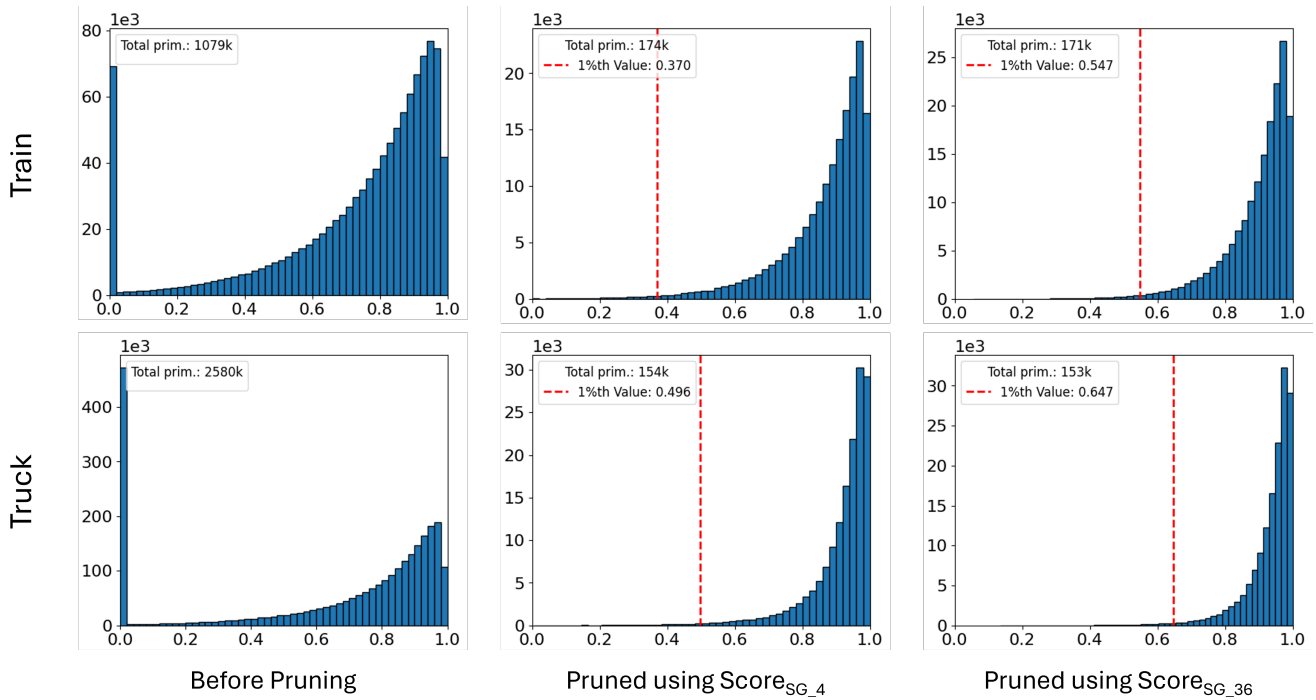


Figure 16. Histogram of primitive’s color similarity over 2 scenes from TanksAndTemples [18]. The X-axis represents color similarity, and the Y-axis shows the number of primitives associated into each bin.

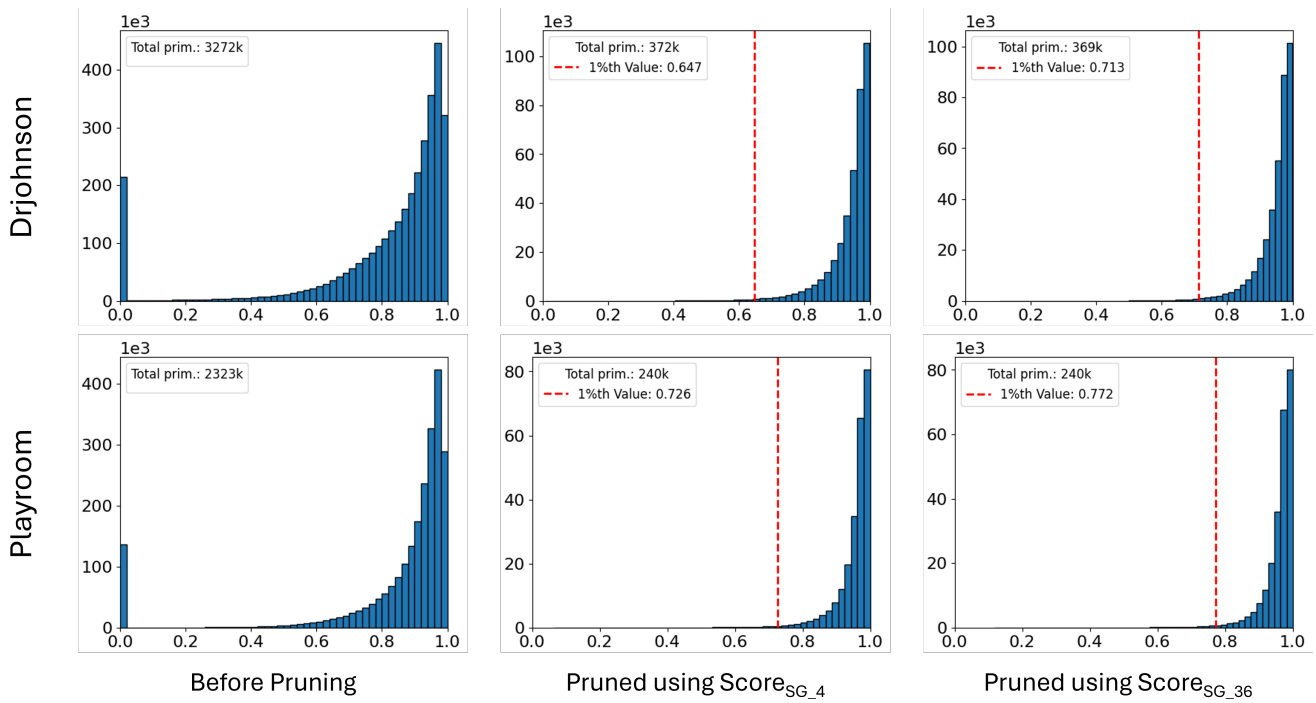


Figure 17. Histogram of primitive’s color similarity over 2 scenes from Deep Blending [15]. The X-axis represents color similarity, and the Y-axis shows the number of primitives associated into each bin.

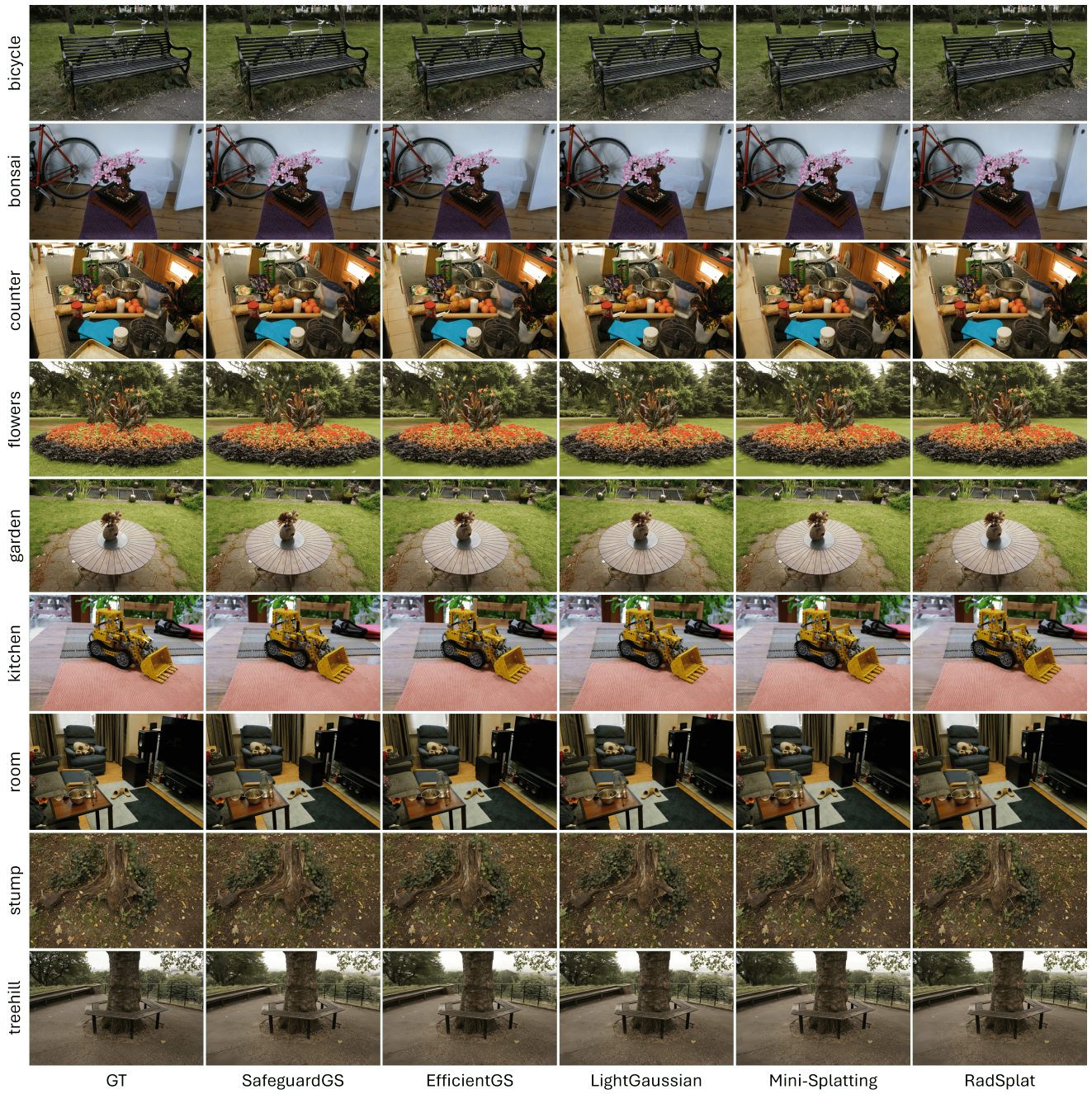


Figure 18. Rendering result of MipNeRF360 [2]



Figure 19. Rendering result of TanksAndTemples [18]



Figure 20. Rendering result of Deep Blending [15]